
Uncertainty Analysis of VAE-GANs for Compressive Medical Imaging

Vineet Edupuganti¹, Morteza Mardani¹, Joseph Cheng^{1,2},
Shreyas Vasawala², John Pauly¹

Department of Electrical Engineering¹ and Radiology², Stanford University
{ve5,morteza,jycheng,vasanawala,pauly}@stanford.edu

Abstract

Reliable medical image recovery is crucial for accurate diagnoses and patient wellbeing. However, high resolution imaging from limited sensory data leaves substantial uncertainty about the authenticity of the recovered pixels. This study aims to quantify this uncertainty so as to guide radiologists about the confidence of their diagnoses. We put forth a probabilistic recovery scheme based on VAE-GANs, comprised of a VAE generator and multi-layer CNN discriminator, that maps out low-quality images with aliasing artifacts to diagnostic-quality ones. We leverage Stein's Unbiased Risk Estimator (SURE) as a proxy for the prediction error, which includes a divergence term (trace of the end-to-end network Jacobian) quantifying the estimation uncertainty. Extensive empirical experiments are performed for the task of magnetic resonance (MR) image recovery using a dataset of pediatric Knee images. We statistically analyze the output distribution of the model using Monte Carlo sampling to gauge the extent of variance, bias, and error across reconstructions. The results indicate that uncertainty level is significantly influenced by the hyperparameter setting and network architecture. The key observations are that the pixel uncertainty level: 1) increases as the GAN loss weight rises; and 2) decreases as we add more recurrent units to the generator network (cascade of VAEs and data consistency layers).

1 Introduction

Solving linear inverse problems is one of the primary challenges in many imaging tasks ranging from natural to medical images. Recovery, however, is typically a daunting task for high resolution imaging because of a lack of sensory measurement due to physical constraints when acquiring data. As such, any image recovery scheme will yield a certain amount of uncertainty regarding the reliability of the recovered pixels.

Though algorithms based on compressed sensing (CS) and especially deep learning (DL) have proven very effective in image recovery, limited work has focused on quantifying uncertainty, exacerbating an already significant lack of experimental methods for determining model robustness [1, 2, 3, 4, 5, 6]. Given the pernicious effects that the presence of image artifacts can have, such methods would have incredible utility both as an evaluation metric and as a way of gaining interpretability regarding risk factors for a given model and dataset [7].

Related work. A small but growing body of work has examined uncertainty in general computer vision problems. Specifically, measurements of uncertainty have been computed by finding the mean and point-wise standard deviation of test images using Monte Carlo sampling, though not for inverse problems in particular [8]. With such a method, comparing the mean intensities of regions containing an artifact and the surrounding area over several cases can provide statistical insights into the types of errors made by the model.

Other studies have explored using invertible neural networks to learn the complete posterior of system parameters [9]. Through bootstrapping, point estimate uncertainty can be obtained statistically and analyzed in a manner similar to posterior sampling. Uncertainty has also been analyzed from the standpoint of data rather than variance introduced by generative models in the context of medical imaging [10]. Techniques such as the bootstrap and jackknife can be used on the sampled input data to produce accurate error maps that provide insight into the most risky ROIs in terms of reconstructions without having access to the ground truth.

Nevertheless, the above approaches are generally constrained by the chosen models or applications and do not apply broadly. Thus, given the nascent stage of this field of research, developing straightforward and effective methods of quantifying uncertainty is incredibly important, with the potential to enable holistic comparison and evaluation of model architectures and hyperparameters across a range of problems.

Contributions. To this end, this work introduces procedures that can provide insights into robustness of DL MR reconstruction schemes. In doing so, we develop a VAE-GAN model for MR image recovery composed of a VAE generator and a multi-layer CNN discriminator. This model is notable for its low error and probabilistic nature which is well-suited to an exploration of model uncertainty. We also employ different loss functions and model architectures to compare results. We first use standard statistical methods to better understand the variations and errors in the output image distribution under different hyperparameter settings [11]. We then proceed to the eigen analysis of the DL model, inspired by SURE as a surrogate for generalization MSE, whereby we explore the singular values of the end-to-end Jacobians over the course of training. Extensive empirical evaluations are performed on real-world medical MR image data. Our key observations include: 1) GAN loss introduces more pixel uncertainty than pixel-wise loss, while better recovering the high-frequencies; 2) the cascaded network architecture better leverages the physical constraint and results in more confident pixels.

All in all, the main contributions of this paper are summarized below:

- A novel VAE-GAN scheme for learning inverse maps
- Quantifying uncertainty using SURE and the eigen analysis of the network Jacobian
- Extensive empirical evaluations with statistical analysis of errors and variance for various network architectures and training losses

The rest of this paper is organized as follows: Section 2 introduces the preliminaries on neural recovery algorithms and states the problem. Section 3 details the VAE-GAN architecture, while generalization risk is analyzed in Section 4. Empirical evaluations are then reported in Section 5, and Section 6 discusses the conclusions and future directions.

2 Preliminaries and Problem Statement

One key application of inverse problems is to Magnetic Resonance Imaging (MRI), which has become a critical healthcare tool over the years due to its unique ability to non-invasively obtain information about tissue composition, structure, and anatomy. As a result, the development of accurate and rapid MRI reconstruction methods could represent a major step forward for the field of medical imaging, with the potential to enable powerful applications like diagnostic-guided surgery or cost-effective pediatric scanning without anesthesia [12, 13]. However, to achieve a high spatiotemporal resolution, significant undersampling is typically employed, leading to challenging image recovery problems.

Specifically, given an observation y , we need to recover an image x , where $y = \Phi x_0$ ($\Phi = \Omega F$, the product of a subsampling mask and the Fourier operator), $y \in \mathbb{C}^m$, $x_0 \in \mathbb{C}^n$, and $m \ll n$, necessitating the use of prior information [14]. One theoretical risk with using DL models in this recovery process, however, is the introduction of realistic artifacts, or so-termed "hallucinations", which can prove costly in a domain as sensitive as medical imaging by misleading radiologists and resulting in incorrect diagnoses [15, 16]. Hence, analyzing the uncertainty and robustness of DL techniques in MR imaging is essential.

Problem statement. More concretely, it stands to reason that there exist multiple recovered images that look both realistic and feasible given a specific data acquisition process. Thus, the objective of this work is to learn a projection onto the intersection between a real image manifold \mathcal{S} and the

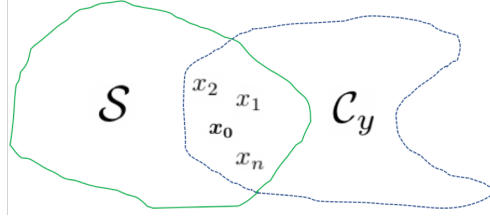


Figure 1: Admissible solutions (x_0 is the true image).

data consistent subspace $\mathcal{C}_y := \{x \in \mathbb{C}^n : y = \Phi x\}$, and understand the uncertainty associated with recovering the true image x_0 (see Fig. 1).

3 VAE-GANs for Medical Image Recovery

For image recovery, we consider a GAN architecture, where the VAE serves as the generator function \mathcal{G} and a CNN as the the discriminator \mathcal{D} . While VAE-GANs have been used successfully in low-level computer vision tasks like super-resolution, they have not been applied to medical image recovery, even though they have the advantage of being able to model high-frequency components that are important in MRI reconstruction [17, 18]. Additionally, the probabilistic nature of this network makes uncertainty analysis especially rich and compelling, which can add a layer of context to radiologist interpretations of recovered images. To deepen our analysis of robustness, we also explore a revised model architecture that is cascaded (i.e. the generator and data consistency portions of the model repeat) for a certain number of "iterations." At test time, latent code vectors were sampled from a normal distribution $z \sim \mathcal{N}(\mu_x, \sigma_x)$ to generate new reconstructions. To ensure that these reconstructions did not deviate from physical measurement, data consistency was applied to all network outputs, which we found essential to obtaining high SNR. Figure 2 depicts the model's components.

The data consistent subspace was obtained by applying an affine projection based on the undersampling mask [18]. The VAE, in turn, was particularly useful to use as a generator function because it learns a probability distribution of realistic images that facilitates the exploration process of the manifold \mathcal{S} . By randomly sampling latent code vectors corresponding to specific images, then, we were able to traverse the space comprising $\mathcal{S} \cap \mathcal{C}_y$ and evaluate the results visually and statistically.

The loss functions used in training were based on the mixture of pixel-wise ℓ_2 and adversarial GAN loss. The constant η was the weight for a KL-divergence term designed to force the latent code (based on μ_x, σ_x for a given batch) to follow a normal distribution [19, 20]. The constant λ served as the GAN weight, controlling the influence of the discriminator. As η increased, the integrity of the generator latent code was preserved at the expense of reconstruction quality. Likewise, as λ increased, the modeling of realistic image components was enhanced but MSE rose. The training cost is formed as:

$$\min_{\Theta_d} \mathbb{E}_x [(1 - \mathcal{D}(x; \Theta_d))^2] + \mathbb{E}_y [(\mathcal{D}(\hat{x}; \Theta_d))^2]$$

$$\min_{\Theta_g} \mathbb{E}_{x,y} (1 - \lambda) [\|x - \hat{x}\|_2^2 + \eta D_{KL}(\mathcal{N}(\mu_x, \sigma_x) || \mathcal{N}(0, 1))] + \lambda \mathbb{E}_y [(1 - \mathcal{D}(\hat{x}; \Theta_d))^2]$$

4 Uncertainty Analysis

4.1 Monte Carlo sampling

An effective way of analyzing uncertainty in computer vision problems is to examine the variability of output images [7]. Nonetheless, this approach has not been applied to inverse problems or medical image recovery. Utilizing the probabilistic nature of the VAE-GAN model, for a given input we can draw samples from the resulting output distribution. This Monte Carlo sampling approach allows one to evaluate variance as well as higher order statistics, which can be very useful in understanding the extent and impact of model uncertainty. However, despite the important information the Monte Carlo approach can provide, some important statistics such as bias are dependent on knowledge of the ground truth, which motivates the next section on SURE.

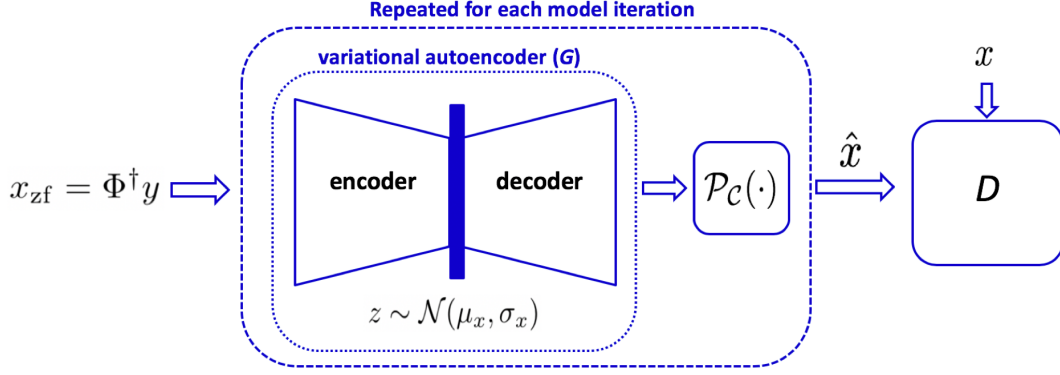


Figure 2: The model architecture, with aliased input images feeding into the VAE encoder, the latent code feeding into the VAE decoder, and data consistency applied to obtain the output reconstruction. This output serves as an input to the GAN discriminator, which in turn sends feedback to the generator. The generator and data consistency layers are repeated in the case of multiple model iterations.

4.2 Denoising SURE

One of the most useful but underexplored statistical techniques for computing risk when the ground truth is unknown is Stein’s Unbiased Risk Estimator (SURE), which has not been used for uncertainty analysis in imaging or DL problems [21]. Given the ground truth image x_0 , the zero-filled image (i.e. the aliased input to the model) $x_{zf} = x_0 + v$, where v is noise, along with reconstruction $\hat{x} = h_\theta(x_{zf})$, where h represents the DL mapping, one can expand test MSE as:

$$\begin{aligned} \mathbb{E}\|\hat{x} - x_0\|^2 &= \mathbb{E}\|x_0 - x_{zf} + x_{zf} - \hat{x}\|^2 \\ &= -n\sigma^2 + \mathbb{E}\|x_{zf} - \hat{x}\|^2 + 2\text{Cov}(x_{zf}, \hat{x}) \end{aligned}$$

SURE finds a surrogate for MSE when the ground truth is unknown. A key assumption behind SURE is that the noise process v that relates the zero-filled image to the ground truth is normal ($v \sim \mathcal{N}(0, \sigma^2 I)$). With this assumption, we can apply Stein’s formula which approximates the covariance to obtain an unbiased estimate of the risk ($\mathbb{E}(\text{SURE}) = \text{MSE}$).

$$\text{SURE} = \underbrace{-n\sigma^2 + \|\hat{x} - x_{zf}\|^2}_{\text{RSS}} + \underbrace{\sigma^2 \text{tr}\left(\frac{\partial \hat{x}}{\partial x_{zf}}\right)}_{\text{DOF}}$$

With the risk expressed in the above form, we can separate the estimate into two terms, with the first term corresponding to residual sum of squares (RSS) and the second one corresponding to degrees of freedom (uncertainty). This form importantly does not depend on x_0 and approximates the DOF with the trace of the Jacobian (gradient of reconstruction with respect to the zero-filled image), which can be easily computed. As such, this attribute will be the primary measure of interest in the later sections of this paper.

4.3 Compressed Sensing (CS) SURE

The primary challenge with the above derivation of SURE is that in reality the noise process v is not always normal. For that reason, we explore Generalized SURE, which is more appropriate for use in compressed sensing, since it is fairly safe to assume that noise produced from measurement is indeed normal [22]. Given our observation y and desired image x_0 with Gaussian noise w , related by $y = \Phi x_0 + w$, reconstructions from our learned model $\hat{x} = f_\theta(y)$, and $P_\Phi = \Phi \Phi^\dagger$ (the orthonormal projection onto the range space of Φ), SURE can be expressed through the following equation. Note that $x_{zf} = \Phi^\dagger y$ and that Generalized SURE is a surrogate for projected MSE ($\mathbb{E}\|P_\Phi x_0 - P_\Phi \hat{x}\|^2$).

$$\begin{aligned} \text{SURE} &= \frac{1}{n} \|P_\Phi x_0\|^2 + \frac{1}{n} \|P_\Phi \hat{x}\|^2 - \frac{2}{n} \hat{x}^T \Phi^\dagger y + \frac{2\sigma_w^2}{n} \text{tr}\left(\frac{\partial \hat{x}}{\partial y}\right) \\ &= \frac{1}{n} \|P_\Phi x_0\|^2 + \frac{1}{n} \|P_\Phi \hat{x}\|^2 - \frac{2}{n} \hat{x}^T x_{zf} + \frac{2\sigma_w^2}{n} \text{tr}\left(\frac{\partial \hat{x}}{\partial x_{zf}} \Phi^\dagger\right) \end{aligned}$$

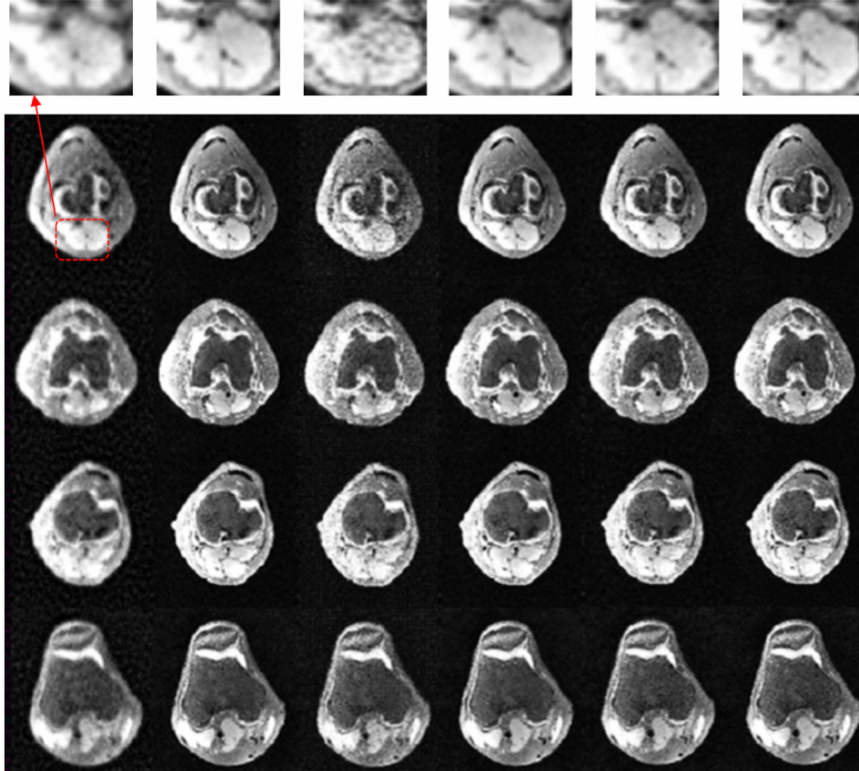


Figure 3: The aliased input, reconstructions with one model iteration and pure MSE loss, one iteration and 10 percent GAN loss, two model iterations and pure MSE loss, and two iterations and 10 percent GAN loss, and the ground truth for four representative slices.

Thus, we see that even if the noise process v in denoising SURE is not Gaussian, the above formulation still contains the same Jacobian uncertainty term (though this time with respect to the measurement). Since Φ^\dagger is known, this quantity can still be computed and has utility across a range of different data acquisition processes [23].

5 Empirical Evaluations

In this section, we assess our model and methods on a dataset of Knee MR images. We first show reconstructions produced with the VAE-GAN model, before demonstrating representative results with the Monte Carlo and eigen analysis methods for quantifying uncertainty.

Dataset. The Knee dataset used for all experiments was obtained from 19 patients with a 3T GE MR750 scanner [24]. Each volume consisted of 320 2D slices of dimension 320×256 that were divided into training, validation, and test examples with a 70/15/15 split stratified by patient, and a 5-fold variable density undersampling mask with radial view ordering (designed to preserve low-frequency structural elements) was used to produce aliased input images x_{zf} for the model to reconstruct [25].

5.1 Network architecture

The VAE encoder was composed of 4 layers formed through a sequence of strided convolution operations followed by ReLU activations and batch normalization [26]. Latent space mean, μ , and standard deviation, σ , were represented by fully connected layers. The VAE decoder also had 4 layers and utilized transpose convolution operations for upsampling [27]. Skip connections were utilized to improve gradient flow through the network [28]. The discriminator function of the GAN was an 8-layer CNN. The use of multiple model iterations whereby the model repeats (generator and data consistency portions) was also explored [29].

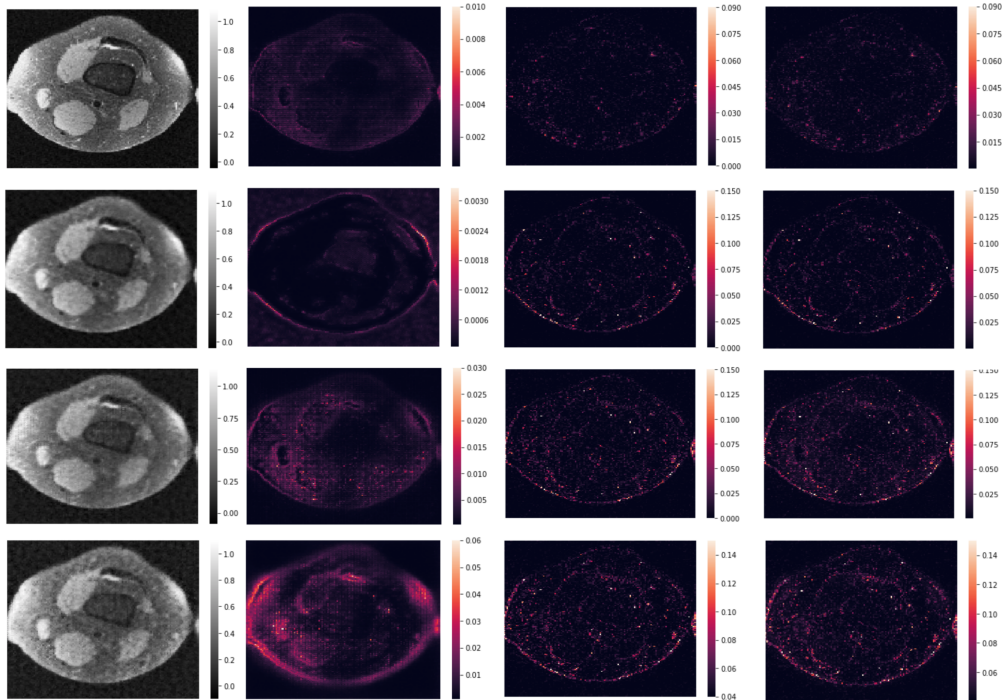


Figure 4: Mean reconstruction, pixel-wise variance, bias, and error for a given reference slice across all realizations. Row 1: 5% GAN loss ($\lambda = 0.05$) with two model iterations. Row 2: 0% GAN loss ($\lambda = 0$) with one model iteration. Row 3: 5% GAN loss ($\lambda = 0.05$) with one model iteration. Row 4: 10% GAN loss ($\lambda = 0.10$) with one model iteration.

Training was completed over the course of 30K iterations, with loss converging over roughly 20K iterations. We utilized the Adam optimizer with a mini-batch size of 4, an initial learning rate of 5×10^{-5} that was halved every 5K iterations, and a momentum parameter of 0.9. Models and experiments were developed using TensorFlow on an NVIDIA Titan X Pascal GPU with 12GB RAM. A version of our TensorFlow source code is publicly available via GitHub [30].

5.2 Individual reconstructions

Figure 3 shows sample model reconstructions (using the mean of the output distribution) for representative test slices with different hyperparameters. As the number of iterations increases from one to two (columns 2 and 3 versus 4 and 5), the resulting outputs improve in quality (corresponding to a roughly 1 dB gain in SNR). Additionally, progressively increasing values of GAN loss (from columns 2 and 4 versus 3 and 5) introduce high-frequency components and artifacts to the image, while leading to sharper outputs. The highlighted ROI elucidates these effects, where the visual degradation associated with poor recovery can be very detrimental to radiologist diagnoses. As expected, the presence of adversarial loss increases average reconstruction SNR (and MSE) as Table 1 shows. With limited GAN loss and additional iterations, though, the SNR is close to 20 dB, indicating that the probabilistic VAE-GAN approach results in low-error image recovery, in addition to facilitating uncertainty analysis.

5.3 Variance, bias, and error maps

Using the Monte Carlo method described earlier, which has not been previously utilized in inverse problems or medical imaging applications, 1K outputs corresponding to different reference slices were generated after training by feeding a test image into the model and sampling from the resulting output distribution.

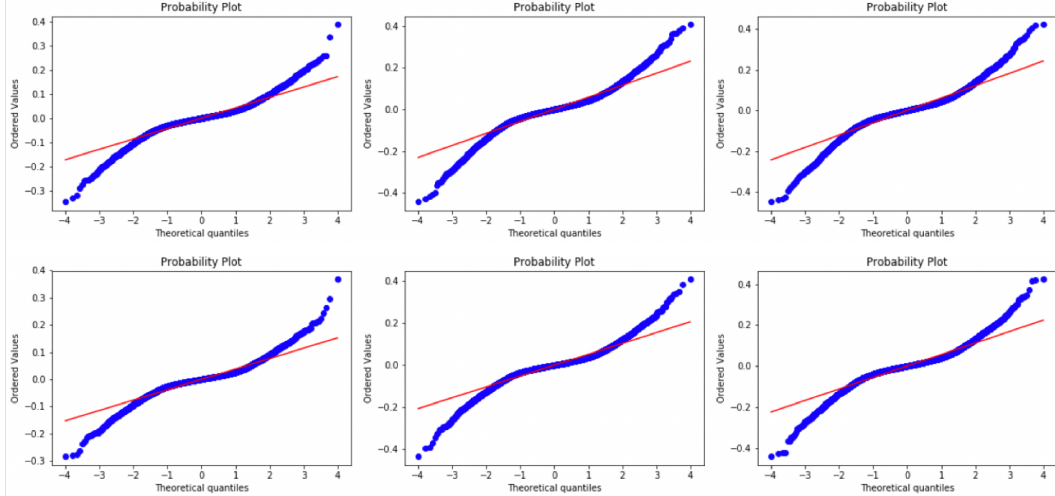


Figure 5: Quantile-quantile plots with 0%, 5%, and 10% GAN loss, respectively, with one model iteration (top row) and two model iterations (bottom row).

We show the mean of the 1K reconstructed outputs for a representative slice and plot the pixel-wise variance, bias (using the mean image as the prediction), and error in Fig. 4, utilizing the common relation $error = bias^2 + variance$ [31]. The concept of bias and variance is important in the analysis of uncertainty because both the difference from the mean and the inherent variability across realizations provide information on the portions of a given image most susceptible to the introduction of realistic artifacts (along with precise numbers that can be used for comparison with different hyperparameter and model schemes).

The results indicate that variance, bias, and error all increase as the number of model iterations decreases (rows 1 and 3) and the GAN loss weight increases (rows 2 through 4). Furthermore in all cases with GAN loss, the variance extends to structural components of the image, which poses the most danger in terms of diagnosis. Nevertheless, with a reasonably conservative choice of GAN weight λ , the risk is substantially lower. Note that these trends were observed with all reference slices that were examined, but we show a single representative example here given that methodological advancements are the primary contribution of this work.

5.4 Noise distribution

While CS SURE is the most relevant form of SURE for inverse problems, it is a proxy for projected MSE, which can be more difficult to interpret than standard MSE. Furthermore, in many situations, one might only have access to input data in the image domain, making it challenging to use CS SURE to compute a useful result. For this reason, we use the Monte Carlo results above to show the validity of denoising SURE, which approximates uncertainty with the end-to-end Jacobians in the image domain, allowing for more widespread use.

As described earlier, the denoising SURE assumption is that the noise process v is normal. To test this assumption, we use the Monte Carlo results from before to generate residuals (difference between reconstructions and zero-filled image). Figure 5 shows the Q-Q plots of these residuals for different conditions. We see that increased GAN loss has the effect of making the residuals slightly more Gaussian, while more model iterations has the opposite effect (though marginal). While the noise distribution is not perfectly Gaussian in any of the cases, we still focus on denoising SURE for the remainder of the paper given that the distributions are sufficiently close for most quantiles and also because of the aforementioned advantages with this method.

5.5 Eigen analysis

Using denoising SURE as in the prior sections, the DOF (trace of the Jacobian $\mathcal{J} := \frac{\partial \hat{x}}{\partial x_{zt}}$) can provide a quantitative metric for analyzing uncertainty when the ground truth is unknown that extends

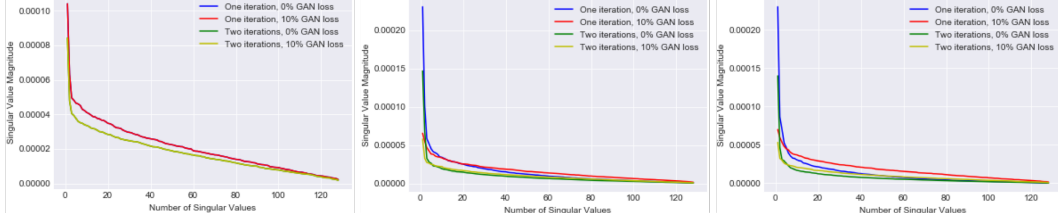


Figure 6: Average singular value magnitudes after 1, 15K, and 30K iterations of training, respectively, for pure MSE loss and 10 percent GAN weight for both one and two model iterations.

Metrics	1 iter., 0% GAN	1 iter., 10% GAN	2 iter., 0% GAN	2 iter., 10% GAN
SNR (dB)	18.82	16.93	19.94	17.88
RSS	0.00072	0.0011	0.00054	0.00087
DOF	0.0015	0.0022	0.00093	0.0012

Table 1: Average SNR, DOF, and RSS for different experimental settings

to deterministic models as well. To evaluate this quantity, we first visualize the Jacobian’s singular values averaged over all reconstructions in Fig. 6 by plotting sorted magnitudes with different model conditions after 1, 15K, and 30K iterations of training (the one model iteration curves overlap in the first plot as do the two iteration ones). By the end of training, we see that the two iteration model with no GAN loss has the smallest singular values. Increased GAN loss and decreased model iterations both result in larger singular value magnitudes, indicating enhanced sensitivity to input perturbations.

The average reconstruction SNR, RSS, and DOF (i.e. the integral of the singular value plots) are shown in Table 1. The RSS was computed using variance maps (not dependent on the ground truth) to approximate σ^2 . Increased GAN loss results in decreased SNR values and increased RSS and DOF. Meanwhile, more model iterations result in higher SNR values and lower RSS and DOF, demonstrating a simple way of improving reconstruction quality while reducing uncertainty. Note that these results align closely with the Monte Carlo analysis from before, thereby reinforcing the effectiveness of the eigen analysis approach in quantifying uncertainty.

6 Conclusions

This paper introduces a series of experimental methods to better analyze uncertainty in compressive MR image recovery. To thoroughly explore realistic and data consistent images, we develop a probabilistic VAE-GAN model, capable of reconstructing and generating medical images with low error. We evaluate the model output distribution statistically in addition to using SURE to motivate examining end-to-end Jacobians and their singular values, a technique that has not been previously demonstrated. We show the utility both these methods can have in terms of gauging uncertainty and serving as a metric of comparison between different models and hyperparameter settings. Furthermore, such insights can directly benefit radiologists by providing more context for diagnoses.

In particular, we note that increased GAN loss leads to larger uncertainty, which is an intuitive result that is important to remember when using adversarial loss to better model high-frequencies in the data. On the other hand, multiple model iterations, whereby the generator and data consistency portions of the network are repeated, decrease uncertainty, which suggests a simple yet effective way of promoting robustness in medical image recovery. Most importantly, the methods presented in this work can be extended beyond inverse problems and to multiple classes of models, including, in the case of eigen analysis, deterministic ones.

Ongoing work is focused on understanding the specific effects of different data acquisition strategies and regularization schemes on DL reconstruction robustness. Future work could involve exploring the effects of network capacity and quantity of training data on model uncertainty.

References

- [1] Alec Radford, Luke Metz, and Soumith Chintala. Unsupervised representation learning with deep convolutional generative adversarial networks. *arXiv preprint arXiv:1511.06434*, 2015.
- [2] Tran Minh Quan, Thanh Nguyen-Duc, and Won-Ki Jeong. Compressed sensing MRI reconstruction with cyclic loss in generative adversarial networks. *arXiv preprint arXiv:1709.00753*, 2017.
- [3] Bo Zhu, Jeremiah Z Liu, Stephen F Cauley, Bruce R Rosen, and Matthew S Rosen. Image reconstruction by domain-transform manifold learning. *Nature*, 555(7697):487, 2018.
- [4] Dongwook Lee, Jaejun Yoo, and Jong Chul Ye. Deep residual learning for compressed sensing mri. In *Biomedical Imaging (ISBI 2017), 2017 IEEE 14th International Symposium on*, pages 15–18. IEEE, 2017.
- [5] Ashish Bora, Ajil Jalal, Eric Price, and Alexandros G Dimakis. Compressed sensing using generative models. *arXiv preprint arXiv:1703.03208*, 2017.
- [6] Ali Mousavi, Ankit B Patel, and Richard G Baraniuk. A deep learning approach to structured signal recovery. In *Communication, Control, and Computing (Allerton), 2015 53rd Annual Allerton Conference on*, pages 1336–1343. IEEE, 2015.
- [7] Alex Kendall and Yarin Gal. What uncertainties do we need in bayesian deep learning for computer vision? In *Advances in neural information processing systems*, pages 5574–5584, 2017.
- [8] Klaus Mosegaard and Albert Tarantola. Monte carlo sampling of solutions to inverse problems. *Journal of Geophysical Research: Solid Earth*, 100(B7):12431–12447, 1995.
- [9] Lynton Ardizzone, Jakob Kruse, Sebastian Wirkert, Daniel Rahner, Eric W Pellegrini, Ralf S Klessen, Lena Maier-Hein, Carsten Rother, and Ullrich Köthe. Analyzing inverse problems with invertible neural networks. *arXiv preprint arXiv:1808.04730*, 2018.
- [10] Mark Tygert, Rachel Ward, and Jure Zbontar. Compressed sensing with a jackknife and a bootstrap. *arXiv preprint arXiv:1809.06959*, 2018.
- [11] Frank E Harrell, Kerry L Lee, and Daniel B Mark. Multivariable prognostic models: issues in developing models, evaluating assumptions and adequacy, and measuring and reducing errors. *Statistics in medicine*, 15(4):361–387, 1996.
- [12] K Hynynen, A Darkazanli, E Unger, and JF Schenck. MRI-guided noninvasive ultrasound surgery. *Medical Physics*, 20(1):107–115, 1993.
- [13] Shreyas S Vasanawala and Michael Lustig. Advances in pediatric body MRI. *Pediatric radiology*, 41(2):549, 2011.
- [14] Michael Lustig, David Donoho, and John M Pauly. Sparse mri: The application of compressed sensing for rapid MR imaging. *Magnetic Resonance in Medicine: An Official Journal of the International Society for Magnetic Resonance in Medicine*, 58(6):1182–1195, 2007.
- [15] Li Xu, Jimmy SJ Ren, Ce Liu, and Jiaya Jia. Deep convolutional neural networks for image deconvolution. In *Advances in Neural Information Processing Systems*, pages 1790–1798, 2014.
- [16] Guang Yang, Simiao Yu, Hao Dong, Greg Slabaugh, Pier Luigi Dragotti, Xujiang Ye, Fangde Liu, Simon Arridge, Jennifer Keegan, Yike Guo, et al. Dagan: Deep de-aliasing generative adversarial networks for fast compressed sensing MRI reconstruction. *IEEE Transactions on Medical Imaging*, 37(6):1310–1321, 2018.
- [17] Anders Boesen Lindbo Larsen, Søren Kaae Sønderby, Hugo Larochelle, and Ole Winther. Autoencoding beyond pixels using a learned similarity metric. *arXiv preprint arXiv:1512.09300*, 2015.

- [18] Morteza Mardani, Enhao Gong, Joseph Y Cheng, Shreyas S Vasanaawala, Greg Zaharchuk, Lei Xing, and John M Pauly. Deep generative adversarial neural networks for compressive sensing (GANCS) MRI. *IEEE Transactions on Medical Imaging*, 2018.
- [19] Alexey Dosovitskiy and Thomas Brox. Generating images with perceptual similarity metrics based on deep networks. In *Advances in Neural Information Processing Systems*, pages 658–666, 2016.
- [20] Diederik P Kingma and Max Welling. Auto-encoding variational Bayes. *arXiv preprint arXiv:1312.6114*, 2013.
- [21] Ryan J Tibshirani and Saharon Rosset. Excess optimism: How biased is the apparent error of an estimator tuned by SURE? *Journal of the American Statistical Association*, pages 1–16, 2018.
- [22] Christopher A Metzler, Ali Mousavi, Reinhard Heckel, and Richard G Baraniuk. Unsupervised learning with stein’s unbiased risk estimator. *arXiv preprint arXiv:1805.10531*, 2018.
- [23] Yonina C Eldar. Generalized sure for exponential families: Applications to regularization. *IEEE Transactions on Signal Processing*, 57(2):471–481, 2009.
- [24] <http://mridata.org/>.
- [25] Joseph Y Cheng, Tao Zhang, Marcus T Alley, Michael Lustig, Shreyas S Vasanaawala, and John M Pauly. Variable-density radial view-ordering and sampling for time-optimized 3d cartesian imaging. In *Proceedings of the ISMRM Workshop on Data Sampling and Image Reconstruction*, 2013.
- [26] Aaron van den Oord, Oriol Vinyals, et al. Neural discrete representation learning. In *Advances in Neural Information Processing Systems*, pages 6306–6315, 2017.
- [27] Simon Jégou, Michal Drozdal, David Vazquez, Adriana Romero, and Yoshua Bengio. The one hundred layers tiramisu: Fully convolutional densenets for semantic segmentation. In *Computer Vision and Pattern Recognition Workshops (CVPRW), 2017 IEEE Conference on*, pages 1175–1183. IEEE, 2017.
- [28] Adji B Dieng, Yoon Kim, Alexander M Rush, and David M Blei. Avoiding latent variable collapse with generative skip models. *arXiv preprint arXiv:1807.04863*, 2018.
- [29] Morteza Mardani, Qingyun Sun, David Donoho, Vardan Papyan, Hatef Monajemi, Shreyas Vasanaawala, and John Pauly. Neural proximal gradient descent for compressive imaging. In *Advances in Neural Information Processing Systems*, pages 9573–9583, 2018.
- [30] <https://github.com/MortezaMardani/GAN-Hallucination/tree/vae>.
- [31] Robert Tibshirani. *Bias, variance and prediction error for classification rules*. Citeseer, 1996.